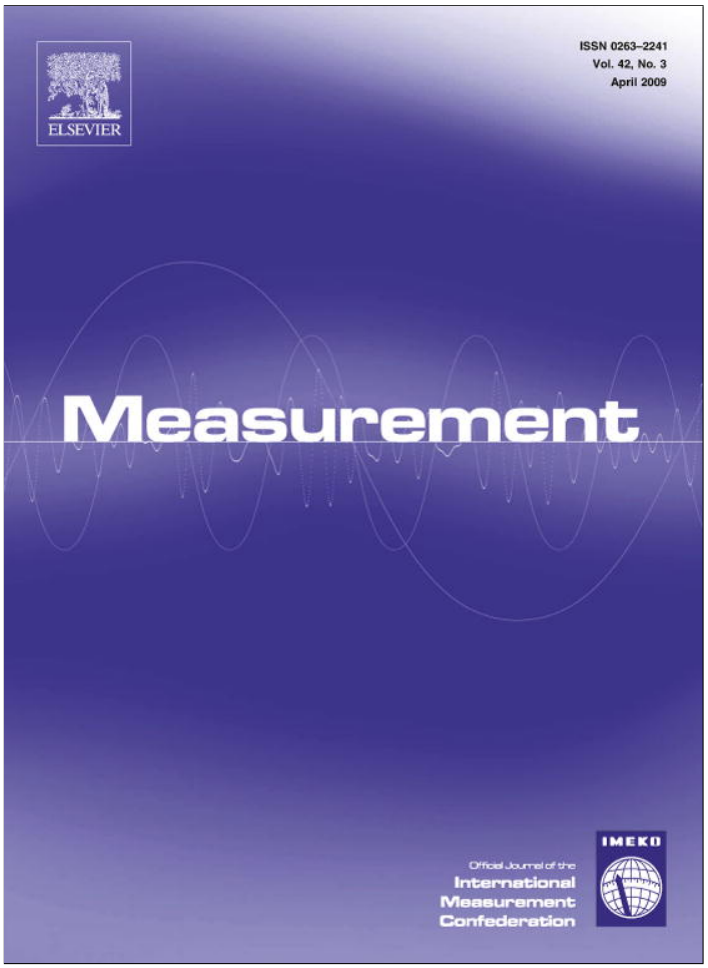

Measurement 42 (2009) 377–389

Contents lists available at ScienceDirect

Measurement

journal homepage: www.elsevier.com/locate/measurement

Near infrared tomographic system based on high angular resolution mechanism – Design, calibration, and performance

Min-Chun Pan [a,*], Chien-Hung Chen [a], Min-Cheng Pan [b], Yi-Ming Shyr [c]

[a] Department of Mechanical Engineering/Graduate Institute of Biomedical Engineering, National Central University, Jhongli, Taoyuan 320, Taiwan
[b] Department of Electronic Engineering, Tung-Nan Institute of Technology, Taipei 222, Taiwan
[c] Department of Surgery, Taipei Veterans General Hospital, National Yang Ming University, Taipei 122, Taiwan

ARTICLE INFO

Article history:
Received 30 October 2006
Received in revised form 19 July 2008
Accepted 1 August 2008
Available online 13 August 2008

Keywords:
NIR diffuse optical tomography
Light intensity measurement
High-resolution scanning device design

ABSTRACT

This study aims at the design, implementation, and verification of a near infrared (NIR) diffuse optical tomography (DOT) electro-optical imaging system based on a measuring instrument with single rotating source/detector scanning mechanism and an image reconstruction scheme implemented on an off-line PC. The developed measurement instrument possesses a high degree of angular resolution and is operated in a continuous-intensity scheme to acquire output NIR intensity signals. In this paper, some considerations of this measuring instrument are investigated such as phantom preparation, temporal stability, and container influence, etc. Experimental trials were conducted using both homogeneous and heterogeneous phantoms made of high-scattering microspheres or Intralipid.

In order to verify the developed imaging system with tomographic image reconstruction, the intensity was acquired from the heterogeneous Intralipid phantom using NIR light at 800 nm, where the homogenous background as the normal tissue is inserted with an inclusion as the tumor. For the comparison of heterogeneous phantoms with homogeneous phantoms, 1-D measured intensity signals indicate the angular position of the inclusion, especially for the case of the inclusion near the phantom boundary. Furthermore, promising results of corresponding optical-property images can be reconstructed with the measured intensities as inputs of the image reconstruction scheme. Obviously, the developed NIR DOT tomographic system has been successfully built upon the experimental, analytical, and computational work.

1. Introduction

Tomography is a medical imaging method of making the interior of the biological tissues visible. At present, there are several tomographic modalities that are widely used to diagnose symptoms and observe physiological reactions. Most of current tomography either has the risk of overexposure like the computed tomography (CT), or poor sensitivity for organic diagnosis. The limited sensitivity of the techniques means that some cancers are difficult or impossible to detect until the tumor is large. For example, the X-ray mammography is the most usual method to detect breast cancer but it is still imperfect since it may take a benign tumor as a malignant tumor; the magnetic resonance imaging (MRI) has the risk of too much magnetic field exposure; and the positron emission tomography (PET) has a cost problem because of the instrument needed for producing short-lifetime radioisotopes. Fig. 1 shows a chronological list of the development on different tomographic modalities including X-ray, CT, MRI, PET, ultrasound imaging and NIR DOT.

NIR tomography has been studied since 1990s and shown to have non-invasive, non-radioactive, and relatively inexpensive properties. Compared with other tomographic modalities, it is, however, not widely used due to its relatively low spatial resolution according to its current technique. But, this tomographic technique with far less

* Corresponding author. Tel.: +886 3 4267312; fax: +886 3 4254501.
E-mail address: pan_minc@cc.ncu.edu.tw (M.-C. Pan).

0263-2241/$ - see front matter © 2008 Elsevier Ltd. All rights reserved.
doi:10.1016/j.measurement.2008.08.003

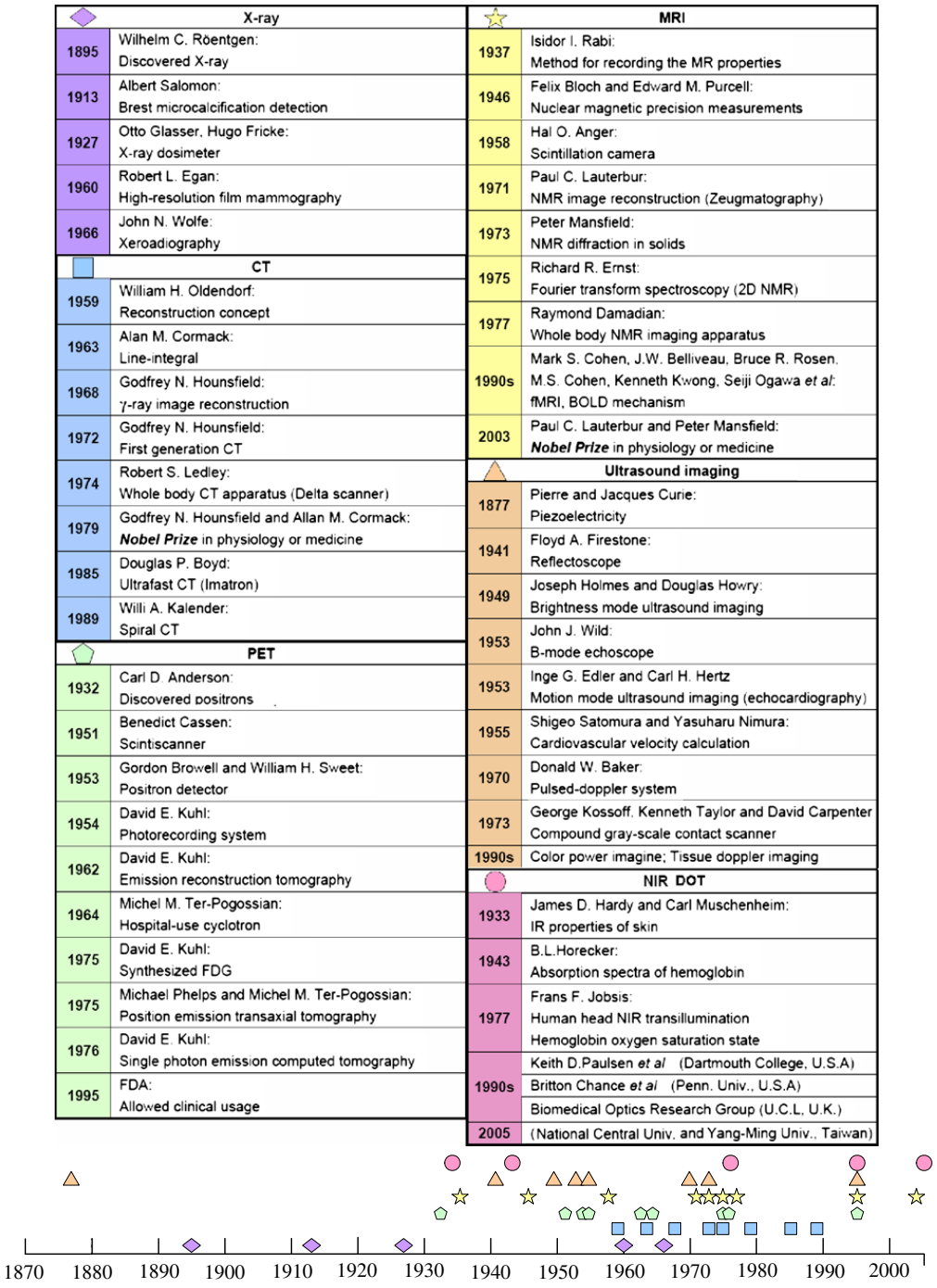

Fig. 1. Chronological list of development on different tomographic modalities including X-ray, CT, MRI, PET, ultrasound imaging and NIR DOT.

risk of overexposure concerns can actually reveal more optical information that differentiates different tissues. Because of the high scattering property of NIR light in tissues, it is more complicated to reconstruct tomographic images than other imaging modalities. Furthermore, the NIR tomographic modality is restricted by the thickness of the phantom or tissue due to the attenuation of the signal with distance through the high scattering material [1]. As mentioned above, these benefits accompanied by negative factors motivate the development and improvement on the NIR diffuse optical tomography (DOT) technique presently. As long as researchers continuously improve on the current drawbacks, it is promising for NIR imaging modality to become a useful tomographic technique in clinic diagnosis eventually [2].

In the present NIR tomographic technique, a finite element (FE) solution of the diffusion equation has been demonstrated to accurately predict the detected light emitted from tissue phantoms, and serves as a basis for the computational reconstruction of images, where NIR tomography has applied to three types of instrumentation, i.e., time domain, continuous wave and frequency domain. Hebden and Wong [3] obtained trans-axial slice images of a cylindrical object containing a highly scattering, low-absorbing

solution by using pico-second pulses of visible light and reconstructed images tomographically. The images were generated by light transmitted through the phantom with the filtered back-projection reconstruction algorithm. Following that, Hebden and Deply [4] proposed an enhanced time-resolved imaging method to remedy the limitation of the available number of photons with sufficiently short paths. Additionally, the MONSTIR system was constructed with a multi-channel time-resolved instrument for tomographic imaging of tissues incorporated with a non-linear diffusion approximation, TOAST algorithm based on FE method [5–8]. Reconstructions can be constrained by using *a priori* information, for example, tissue boundaries [9]. The instrument of continuous wave as implied by the name is using continuous wave (CW or DC) light as a light source where the measurement of emerging light can yield the wavelength dependent attenuation, and absorption images can be obtained by measuring intensities around the tissue boundary along with the image reconstruction scheme [10–15], in which Paulsen et al., Schmitz et al. and Hielschera et al. have conducted bunch of works with the architecture of fixed number of source–detector combination. Choe [16] developed clinical DOT with multi-source and multi-detector for *in vivo* breast cancer imaging. McBride et al. [17] developed a frequency domain optical tomography system utilizing a Ti–S laser system at different wavelengths of 700, 800, and 830 nm modulated at 100 MHz, and a single PMT detector, where both are serially illuminated by each source or detector fiber on a sliding stage, respectively. A frequency-domain system uses sinusoidal amplitude-modulated light sources. Comparison of the source signal and detector signal reveals the phase lag and the attenuation of amplitude and thus reconstructed images can be computed [15,18]. A comparison among the above instrumentation can also be seen in Ref. [13].

For the former NIR DOT systems with 16S/16D (S, source; D, detector) or 25S/32D fiber bundle scheme [13,17,19], this structural configuration benefits data-acquiring speed; on the other hand, these systems offer less flexible operation. More precisely, 16 (or 25) input sources and 16 (or 32) output intensities restrain spatial resolution while they scan around a specific circumference. Using these systems to scan a phantom with large diameter, coarse spatial resolution will be obtained. Furthermore, the minimum diameter of a phantom to be detected is limited by the geometric dimension of fiber bundles. The study aims at the design, implementation, and verification of an NIR DOT electro-optical imaging system based on a measuring instrument with a single rotating source/detector scanning mechanism and an image reconstruction scheme implemented on an off-line PC. The developed measuring instrument possesses a high degree of angular resolution, and is operated in a continuous-intensity scheme to acquire output NIR intensity signals. In the study, some considerations of this measuring instrument are investigated such as phantom preparation, temporal stability, and container influence, etc. Experimental trials were conducted using both homogeneous and heterogeneous phantoms made of high-scattering microspheres or Intralipid. Following the above brief introduction, this paper is organized as follows. Section 2 describes the developed NIR imaging system including a measuring instrument and image reconstruction scheme. Section 3 discusses phantom preparation and some considerations on the measuring instrument. Next, experimental results are presented in Section 4 to show photon density wave, forward intensity measurement and numerical image reconstruction. Finally, in Section 5 some remarks are concluded on the current imaging system.

2. NIR DOT imaging system

Basically, an NIR DOT imaging system is composed of a measuring instrument associated with image reconstruction scheme for the purpose of reconstructing NIR optical-property tomographic images of the phantoms of interest. The reconstructed images reveal the NIR optical properties of tissues computed by using measured intensities emitted from the circumference of the object. In this section, the hardware configuration with highly angular resolution and the basic theory of image reconstruction are described as follows.

2.1. Hardware configuration

The NIR measuring instrument with highly angular resolution in the research adopts rotating mechanism based on a single source and detector, as shown in Fig. 2, where the scanning device is rather economical and easily implemented. Additionally, the angular resolution of the measuring instrument can be flexibly tuned by predefining the step angle as small as expected, which is much better than former systems employing the fixed source-and-detector pairs. Fig. 2 illustrates the schematic diagram, design and photograph of the scanning device, where Fig. 2(a) shows the design diagram of rotational scanner which consists of two driving motors and two arms for fiber-mounting. Two stepping motors (StepSyn 2-Phase stepping motor, Sanyo Denki, Ueda, Japan) with an angular resolution of 1.8°/step transmit power through worm-gear sets. Thus, the operating resolution of the scanning can be as high as 0.02°/step. One optical fiber mounted on each rotating arm is to illuminate light source, or collect out-emitted intensities. The radial and vertical positions of each fiber can be manually adjusted against the phantom. The size of the detected phantom placed between two optical fibers can reach up to 10.8 cm of diameter at the current design.

In the scanning operation, the step angle is predefined as 5° to acquire about 60 intensity data for each of 16 source positions. The whole data acquisition time takes under 25 min for a single tomographic slice. Intensity data between ±20.0° around the light source are not available due to the limitation of the interference of the source and detector in the current design. These ignored data are subsequently obtained by extrapolating the measured data.

The NIR emitting and acquiring instrument mainly comprises a laser diode (LD) (SDL-5412-H1, JDS Uniphase Corp., CA, US) at 800 nm as the light source, which is driven by a DC current source (LDI-800, Laser Drive Inc., PA, US)

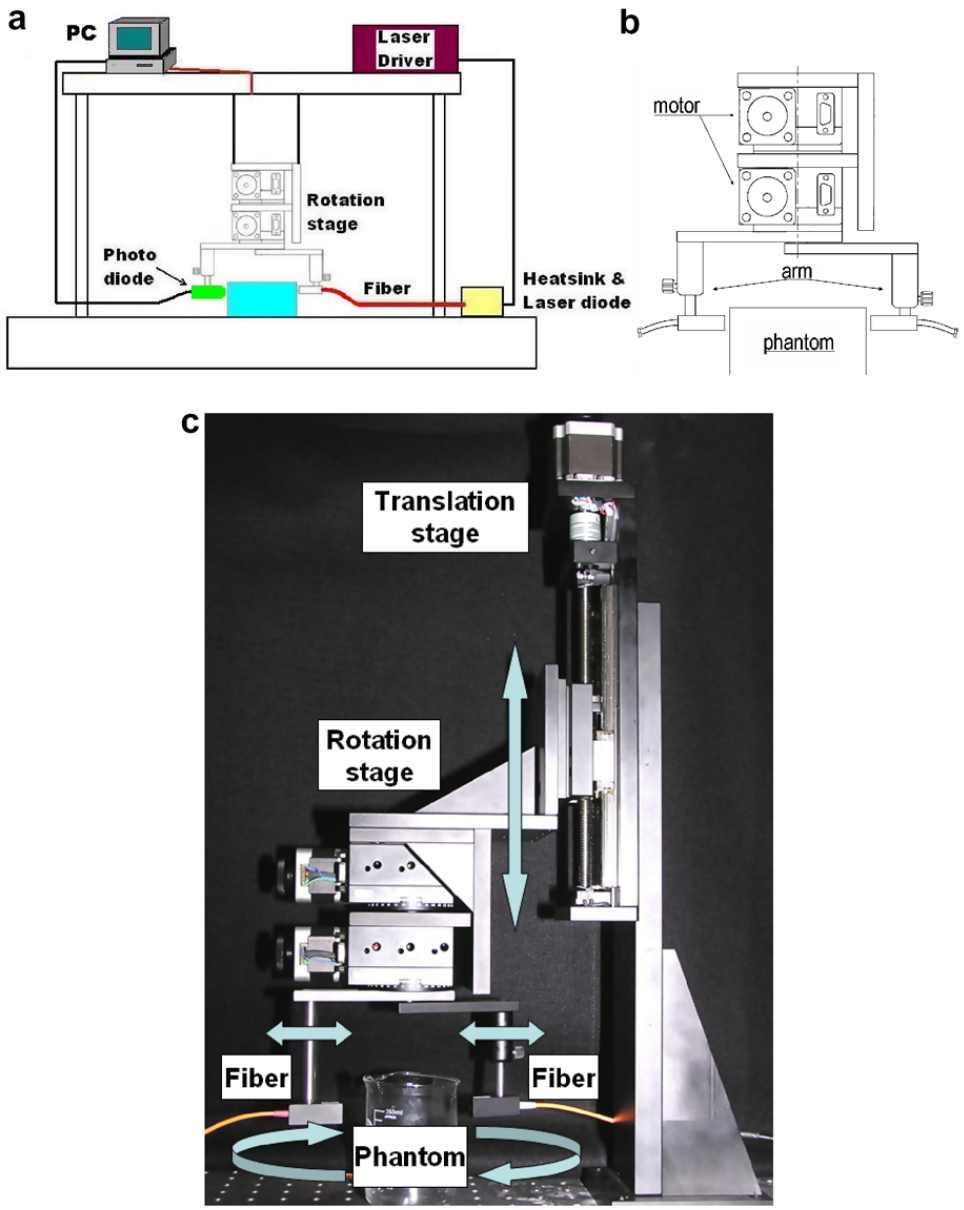

Fig. 2. (a) Schematic diagram, (b) design and (c) photograph of the developed NIR scanning device based on a single rotating source/detector.

and temperature-controlled by a heat-sink component (LDI-800-H, Laser Drive Inc., PA, US). The LD is mounted in the heat-sink with a fiber coupler (OZ Optics, ON, Canada). The output intensities are collected by an optical fiber (OZ Optics, ON, Canada), and a photo diode (SDO Communications Corp., Taiwan) as the detector. Subsequently, a 12-bits DAQ equipment (6064E DAQ-Card, National Instrument, Austin, TX, US) samples and stores data to a host PC. For up-to-command tuning data-acquiring parameters and operating the source/detector scanning device, a human-machine interface is programmed through the LabVIEW™ (National Instrument, Austin, TX, US), a graphical programming development environment. Compared with other NIR intensity measuring devices using a fiber-holder ring or radial movement mechanism with a fixed number of input and output fibers [6–8,13–15,18,19], the scanning device is rather flexible and economical, thereby dramatically saving source and detector fiber-bundles and offering even better spatial resolution for next stage of image reconstruction. For the measuring instrument and dedicated desk-top computer, they cost only around US$ 20,000 and the program of inverse solution developed with MATLAB™ is in-house coded.

2.2. Image reconstruction scheme

In the image reconstruction, both forward and inverse computations are investigated. The forward computation is to obtain the intensity out of a phantom for a given source, and the initial-guess (or iterated) scattering and absorption coefficients; the inverse computation, to compute the scattering and absorption coefficients for a known light source and measured intensities. The modeling described here is using light propagation through diffusive media via diffusion approximation to the Boltzmann equation.

In the study, image reconstruction is based on the diffusion equation and the finite element method, and sought from boundary-value measurements to validate the setup of developed imaging system. As described previously, the physical process can be derived from a diffusion equation

$$\nabla \cdot D\nabla\Phi(r,\omega) - \left(\mu_a - \frac{i\omega}{c}\right)\Phi(r,\omega) = -S(r,\omega) \tag{1}$$

where $S(r,\omega)$ and Φ denote the source and the intensity, respectively. μ_a, c and D are the absorption coefficient, the wave speed in the medium and the diffusion coefficient, respectively. For solving Eq. (1), the boundary condition, $-D\nabla\Phi\cdot\hat{n} = Flux = \alpha\Phi$, and the finite element method are applied. Thus the following discrete equations in a matrix form can be obtained:

$$\begin{bmatrix} A_{ij}^{bb} - \alpha B_{ij}^{bb} & A_{ij}^{bI} \\ A_{ij}^{Ib} & A_{ij}^{II} \end{bmatrix} \begin{Bmatrix} \Phi_j^b \\ \Phi_j^I \end{Bmatrix} = \begin{Bmatrix} C_i^b \\ C_i^I \end{Bmatrix} \tag{2}$$

Obviously, the forward solution, Φ, can be evaluated through Eq. (2). Furthermore, the following two equations can be derived for the computation of image reconstruction, i.e.

$$\begin{bmatrix} A_{bb} - \alpha B_{bb} & A_{bI} \\ A_{Ib} & A_{II} \end{bmatrix} \begin{Bmatrix} \frac{\partial\Phi_b}{\partial D_k} \\ \frac{\partial\Phi_I}{\partial D_k} \end{Bmatrix} = \begin{bmatrix} -\frac{\partial A_{bb}}{\partial D_k} & -\frac{\partial A_{bI}}{\partial D_k} \\ -\frac{\partial A_{Ib}}{\partial D_k} & -\frac{\partial A_{II}}{\partial D_k} \end{bmatrix} \begin{Bmatrix} \Phi_b \\ \Phi_I \end{Bmatrix} + \begin{Bmatrix} \frac{\partial C_b}{\partial D_k} \\ \frac{\partial C_I}{\partial D_k} \end{Bmatrix}, \tag{3}$$

and

$$\begin{bmatrix} A_{bb} - \alpha B_{bb} & A_{bI} \\ A_{Ib} & A_{II} \end{bmatrix} \begin{Bmatrix} \frac{\partial\Phi_b}{\partial \mu_l} \\ \frac{\partial\Phi_I}{\partial \mu_l} \end{Bmatrix} = \begin{bmatrix} -\frac{\partial A_{bb}}{\partial \mu_l} & -\frac{\partial A_{bI}}{\partial \mu_l} \\ -\frac{\partial A_{Ib}}{\partial \mu_l} & -\frac{\partial A_{II}}{\partial \mu_l} \end{bmatrix} \begin{Bmatrix} \Phi_b \\ \Phi_I \end{Bmatrix} + \begin{Bmatrix} \frac{\partial C_b}{\partial \mu_l} \\ \frac{\partial C_I}{\partial \mu_l} \end{Bmatrix}. \tag{4}$$

The Newton–Raphson technique regularized by a Levenberg–Marquardt algorithm is adopted for iteratively updating the diffusion and absorption coefficients, i.e.,

$$(J^TJ + \lambda I)\Delta\chi = J^T(\Phi^o - \Phi^c) = J^T\Delta\Phi \tag{5}$$

where Hessian matrix J denotes $J(\frac{\partial\Phi_b}{\partial D_k}, \frac{\partial\Phi_b}{\partial\mu_l})$, $\Delta\chi$ means $\Delta\chi(\Delta D_k, \Delta\mu_l)$ and λ is a regularization parameter for Tikhonov regularization of the Hessian matrix. Fig. 3 illustrates the procedure of image reconstruction scheme for the computation of optical properties.

In the simulation, a boundary-condition constant (α) is chosen to be a unit and a regularization parameter (λ) is adopted with scaling the maximum of absolute values of matrix J with a factor (0.75) for each iteration. Some more details can be found in Paulsen and Jiang's work [15]. According to the previous experience, it is found that image reconstruction can be accomplished with 8 sources by 16 detectors combination as well, but not performs well with only 4 sources by 16 detectors combination. In spite of this fact, 16 by 16 sources/detectors combination is still recommended. The reconstruction resolution is actually dependent of the source–detector combination. Additionally, our numerical scheme is robust to various situations [20] in spite the information illustrated here is qualitative rather than quantitative.

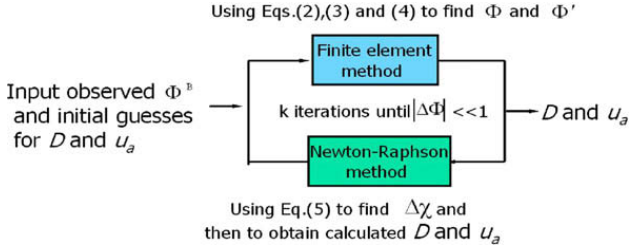

Fig. 3. Procedure of image reconstruction scheme.

3. Instrumentation considerations

In the experiments, phantoms that mimic different NIR optical properties of tissues have been conducted by using hemoglobin, microspheres, and Intralipid. This section addresses their preparations. Additionally, considerations on the measuring instruments such as temporal stability, container influence and so on are investigated for the purpose of performing experiments well.

3.1. Phantom preparation

Phantom preparations about recipes and mixing procedure are described as below.

3.1.1. Hemoglobin phantom

To produce a hemoglobin phantom is rather complicated by dissolving commercial hemoglobin powder in distilled water. The oxidization of aqueous hemoglobin solution may take place quickly. This makes hemoglobin (clear red) oxidization happen and become methemoglobin (brown). For an obtaining stable hemoglobin phantom, some sophisticated steps are needed [21].

3.1.2. Microsphere phantom

One popular material for the preparation of tested phantoms is microsphere polymer powder ranging from 1 to 50 μm in diameter. Microsphere is a high-scattering medium and its absorption and scattering characteristics can be controlled by mixing with water or ink. As expected in Fig. 4(a), the measured NIR intensity from the tested phantom is like a smiling curve, but the settling problem of microspheres appears during the measurement process. Thus this unwanted influence needs to be coped with. Sodium hexametaphosphate $(NaPO_4)_6$, a kind of industrial dispersant, is used and mixed with microsphere liquid. Then, a stable NIR intensity around the tested microsphere phantom for lasting several hours can be obtained, as shown in Fig. 4(b).

3.1.3. Intralipid phantom

Compared with polystyrene microspheres or hemoglobin, Intralipid is a suitable material for phantoms with two main advantages. One is affordability: microspheres cost ten times more than Intralipid, and the other is flexibility: the scattering coefficient of Intralipid is large enough to imitate NIR characteristics of different human tissues by dilution. Additionally, microspheres have the

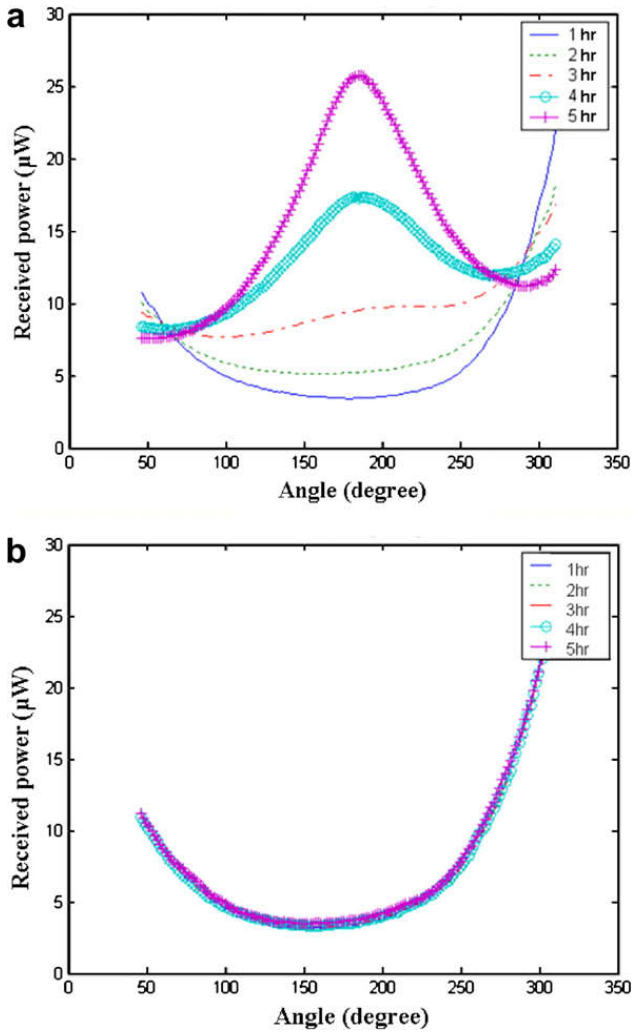

Fig. 4. $(NaPO_3)_6$ buffer effect on the measured intensities of the microsphere phantom; (a) without adding $(NaPO_3)_6$ buffer, and (b) with $(NaPO_3)_6$ buffer added.

effect of settling that makes phantoms unsteady although $(NaNO_4)_6$ can be used.

There are two types of commercial Intralipids: Intralipid-10% and Intralipid-20% that represent the solution of Intralipid mainly consisting of 10% and 20% soybean oil, respectively. Van Staveren et al. [22] proved that the scattering spectrum of Intralipid-10% is approximately decreasing as the wavelength increases. The scattering coefficient of Intralipid-10% is much larger than human tissues, and this Intralipid can simulate the scattering property of the tissue by reducing the concentration of Intralipid-10%.

In the study, 1% Intralipid is prepared by mixing 10 volumes of Intralipid-10% and 90 volumes of water. Thus the process of preparing *z%* Intralipid is described in items as below:

(1) Deciding the volume of water and Intralipid: 100 mL of *z%* Intralipid contains 10z mL of Intralipid-10% and (100–10z) mL water, respectively;
(2) Diluting: Use the burette to measure 10z mL of Intralipid-10% and (100–10z) mL of water, and then mix them well in a beaker.

3.2. Influencing factors on measurement

Considerations on instruments that may influence experimentation are crucial for obtaining reliable results. In the study, the temporal stability of laser diodes, variation of in-house-made containers, and intensity attenuation in air, water, ink and Intralipid are considered.

3.2.1. Temporal stability of laser diodes

As the working temperature of the laser diode is controlled by a heat-sink component, the input power stability relates to hear-sink temperature while the temperature of heat sink is varying, consistent light source will be not available. Fig. 5 charts the heat-sink temperature in °C and the corresponding output power of NIR illumination detected by an optical power meter (Nova, Ophir Optronics Inc., MA, US) for a period of 1 hour after power on. Obviously, it indicates that warm-up time of around 45 min is required to fully stabilize the light source.

3.2.2. Variation of in-house-made containers

In the experimentation, the liquid phantoms are not always contained in a beaker made of specific optical glass. In-house-made containers made of transparency were employed for most experiments. The influences of transparency containers on measurement need to be considered for subsequent optical-property image reconstruction. An incident light through the container includes three parts, reflection, refraction and absorption. The transmittance of the transparency used here is ranging from 90% to 92% of the source power, as shown in Fig. 6.

3.2.3. Attenuation in air water, ink, and Intralipid

Air gap exists between the tip of the detector-fiber and tested phantom, and its influence on light attenuation is measured, as shown in Fig. 7. It is noted that while air gap is less than 20 mm the attenuation influence can be ignored. The power loss rate is around 1% input power per cm.

The attenuation of an incident light with input intensity I_0 through media such as biological tissues is described by

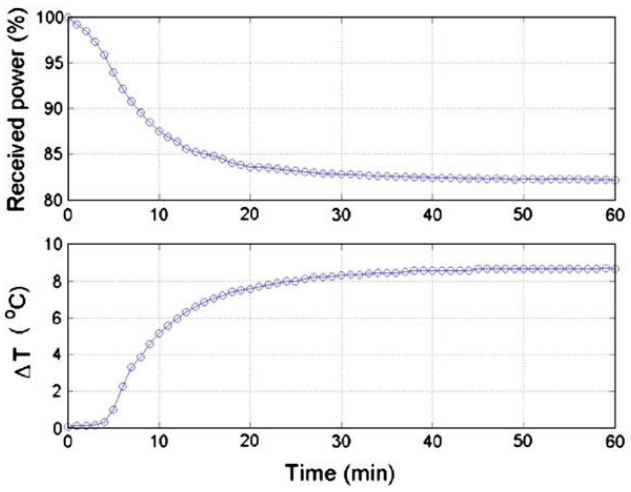

Fig. 5. Illustration on the temporal stability of NIR light source.

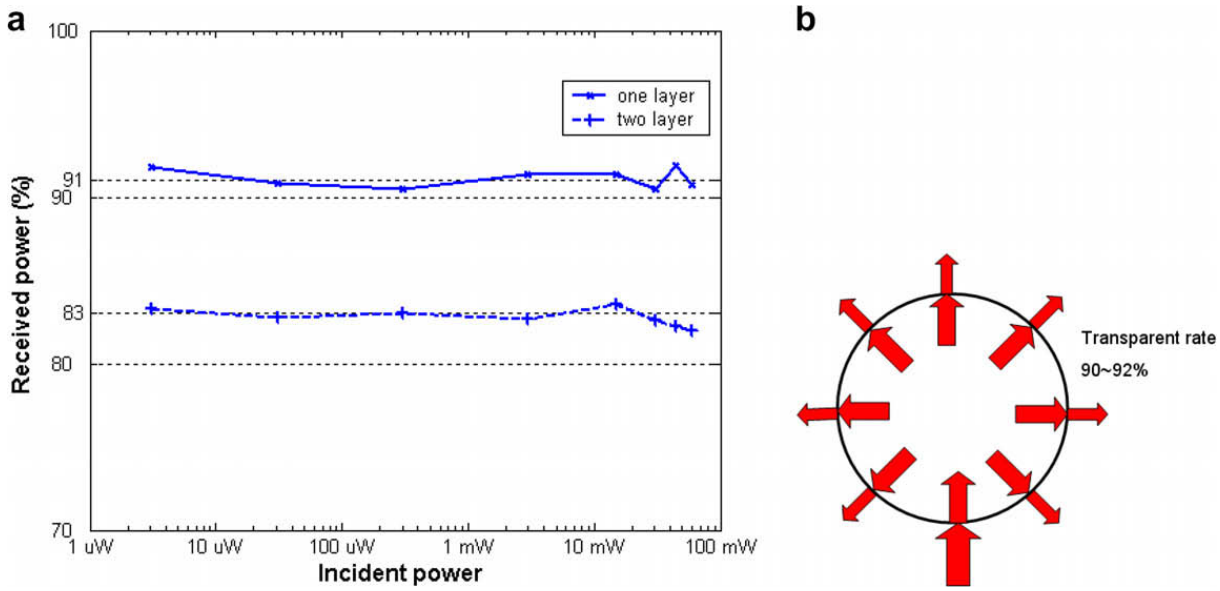

Fig. 6. Influence of the transparency container on NIR light measurement. (a) Attenuation rate through the transparency container, (b) attenuation diagram for the transparency container.

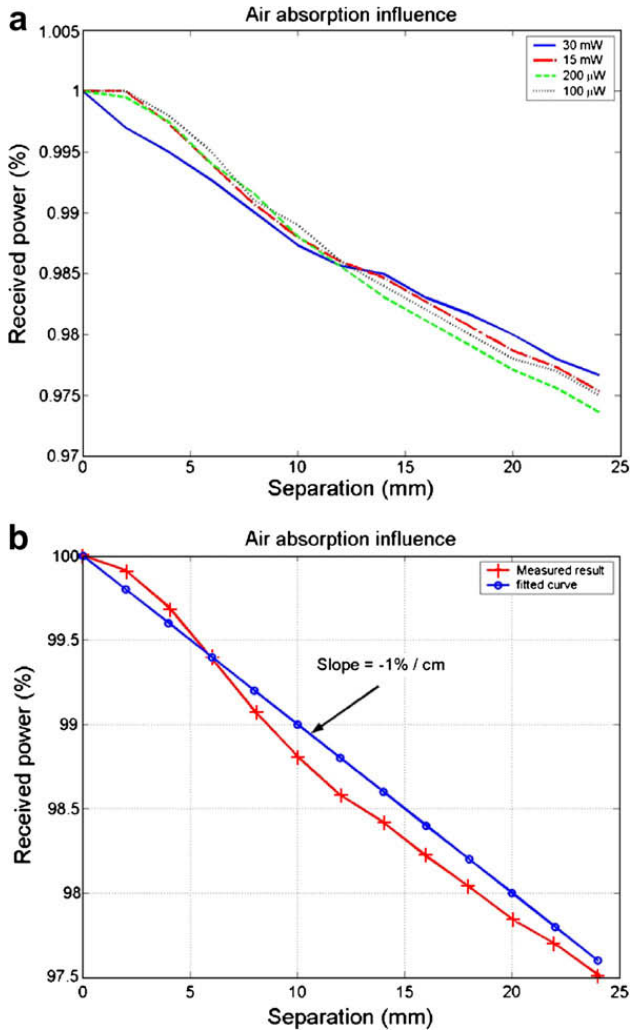

Fig. 7. Influence of air absorption on NIR light intensities. (a) Air absorption at various input power; (b) averaged air absorption and fitting curve.

$$I = I_o \exp[-(\mu_{a+}\mu_s)ct] = I_o \exp(-\mu_{\text{ext}}c), \tag{6}$$

where μ_{ext} ($\text{mm}^{-1}\,\text{mL}^{-1}\,\text{L}$) denotes the extinction (attenuation) coefficient, c ($\text{mL}\,\text{L}^{-1}$) the concentration of the volume density, and t (mm) the geometrical path length in the sample phantom. Here, concentration is defined as the ratio between the volume (in milliliters) of the solution (Intralipid-10%) and the total volume (in liters) of solution plus solvent (water). For instance, one-percent volume density (v.d.) defined as previous; i.e. 1% (v.d.) equal to 100 $\text{mL}\,\text{L}^{-1}$ Intralipid-10%. As depicted, the slope of a plot of $\ln(I/I_o)$ versus (ct) can determine the attenuation coefficient, μ_{ext}. Since all measured power intensity have been normalized to I_o, additional absorption or scattering by water has virtually no influence on the value of the experimental extinction coefficients.

Fig. 8 shows the device designed for the measurement of intensity attenuation such as for water, ink and Intralipid. Figs. 9 and 10 demonstrate the NIR optical characteristics of ink and Intralipid at various concentrations, respectively. The attenuation of light through ink solution, as shown in Fig. 9 characterizes normalized intensity (I/I_o) versus phantom thickness (t: mm) and the multiplication of

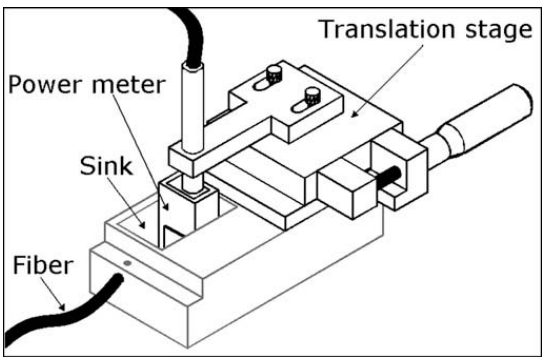

Fig. 8. Device for the measurement of liquid attenuation.

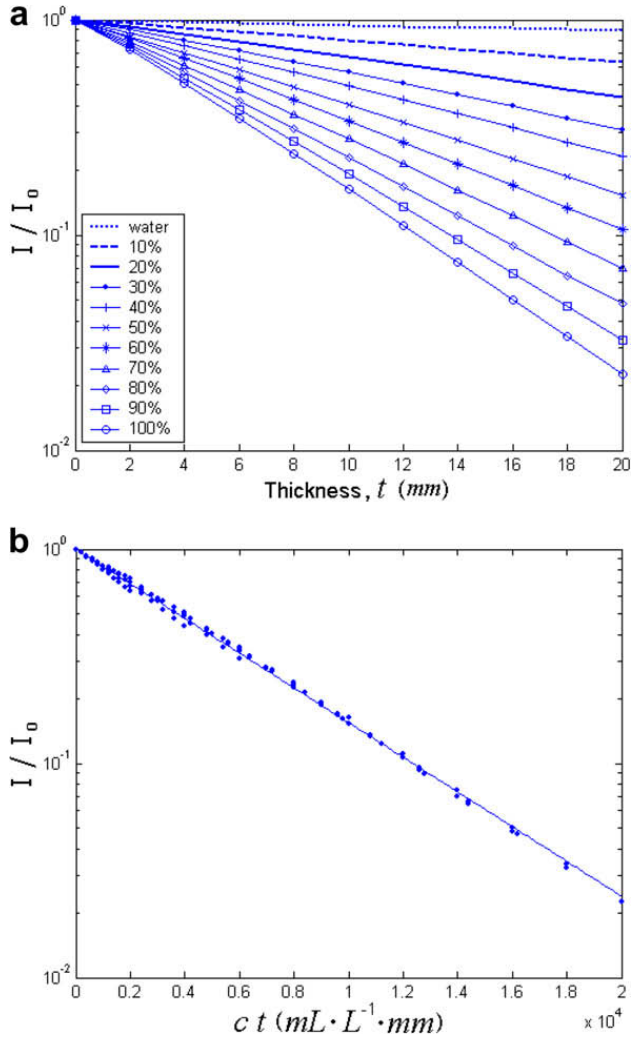

Fig. 9. Intensity power attenuation through ink at various concentrations.

concentration and phantom thickness (ct: mL L^{-1} mm). A fitting curve shown in Fig. 9(b) as Eq. (6) is simply found with μ_{ext} =0.0001865 mm^{-1} mL^{-1} L (or 0.1865 mm^{-1}) and σ =0.0000135 mm^{-1} mL^{-1} L (or 0.0135 mm^{-1}). As to Intralipid, Fig. 10 shows normalized intensity (I/I_o) versus phantom thickness (t: mm) and the multiplication of concentration of phantom thickness (ct: mL^{-1} L mm). A fitting curve shown in Fig. 10(c) for v.d. below 0.2% is simply found by using μ_{ext} = 0.0123 mm^{-1} mL^{-1} L (or 12.3 mm^{-1}) and σ = 0.0025 mm^{-1} mL^{-1} L (or 2.5 mm^{-1}).

4. Optical-property image reconstruction using acquired intensities

In this section, the photon density wave of NIR light interacting with the microsphere phantom will be shown to illustrate a clear view of light distribution in the highly scattering medium. Acquired intensities out of test phantoms and subsequent image reconstruction are discussed. Highly angular resolution compared with the result from the design using fixed source-and-detector pairs shows the merits of the developed scanning device. Reconstructed optical-property images using the measured data

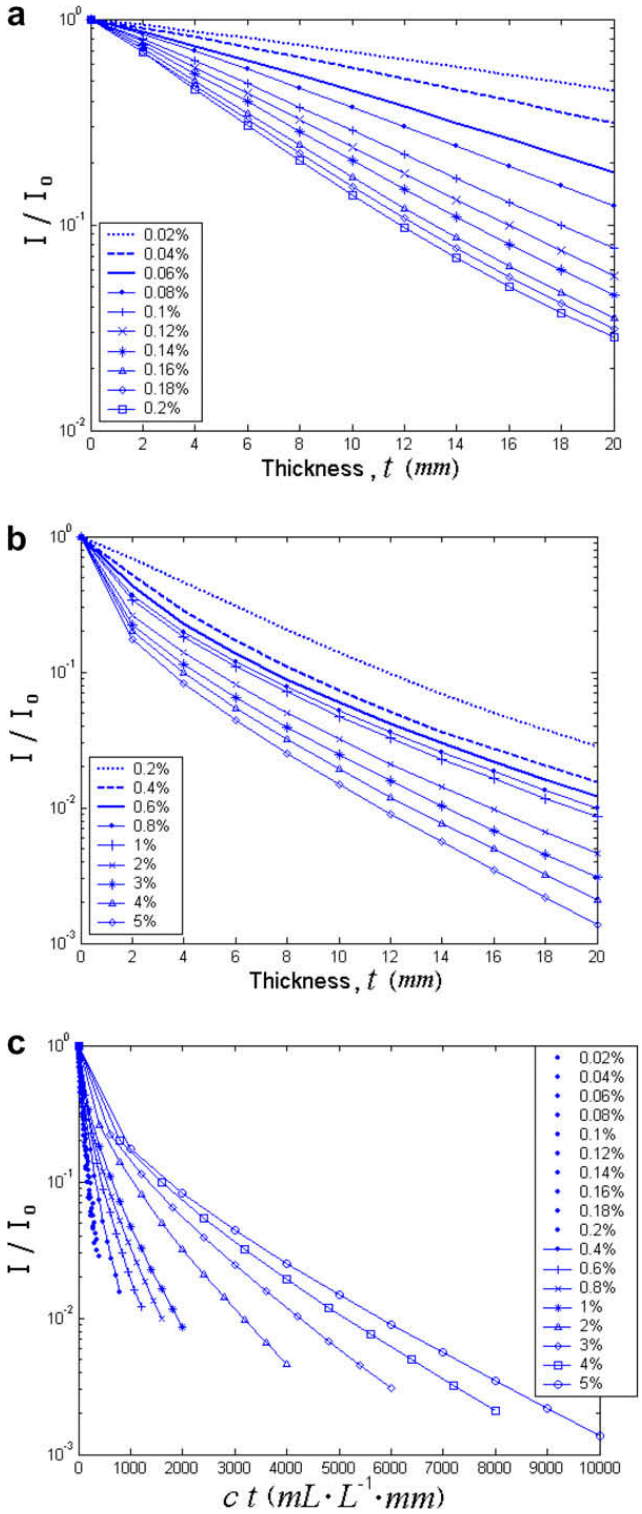

Fig. 10. Intensity attenuation through Intralipid at various concentrations.

of the heterogeneous Intralipid phantom further validate the imaging system.

4.1. Photon density wave

The phenomenon of NIR light transmitting through a high scattering phantom is quite different from through a

low scattering medium. As shown in Fig. 11, the photographs show the NIR light illumination through 0.95% and 1.9% v.d. of homogenous microsphere phantoms. It is noted that light intensity in the low v.d. phantom goes through further than in the high v.d. phantom. Thus it is expected that larger acquired data can be obtained surrounding the circumference of the low v.d. phantom.

4.2. Forward intensity measurement

In the experiment, a circular phantom (100 mm) with one inclusion (10 mm) was placed at 0° and off-centered 40 mm. The homogeneous Intralipid background with μ_s = 0.07 mm^{-1} and μ_a 0.002 mm^{-1} employed as a normal tissue was inserted with an inclusion with μ_s 10 mm^{-1} and μ_a 0.0085 mm^{-1} as a 'tumor'. An NIR Laser diode was used as source excitation a power of 70 mW and a wavelength at 800 nm. Fig. 12 demonstrates the measurements of incident NIR light through the Intralipid phantom, where intensity is in arbitrary unit and angle is from source to detector. As shown, Fig. 12(a)–(p) are measured 1-D intensity signals surrounding the homogeneous and heterogeneous phantoms. It can be seen that the deviation position of the heterogeneous phantom from the homogeneous indicates the angular orientation of inclusion. Furthermore, the deviation arising from the inclusion depends on the inclusion size in spite of the dependence upon the optical properties as well.

As described previously, the measurement instrument inherits the feature of highly angular resolution. For the demonstration of this merit, as shown in Fig. 13, the experimental measurements are compared with those acquired from the instrument with fixed source-and-detector pairs which were obtained by selecting the measurements at 16 fixed positions for each source position. Note that the difference at the position pointed with an arrow by comparing the first row with the second row, or the third row with the fourth row. Apparently, the features of the second and fourth rows are more visible. These sound features are helpful for the subsequent image reconstruction task.

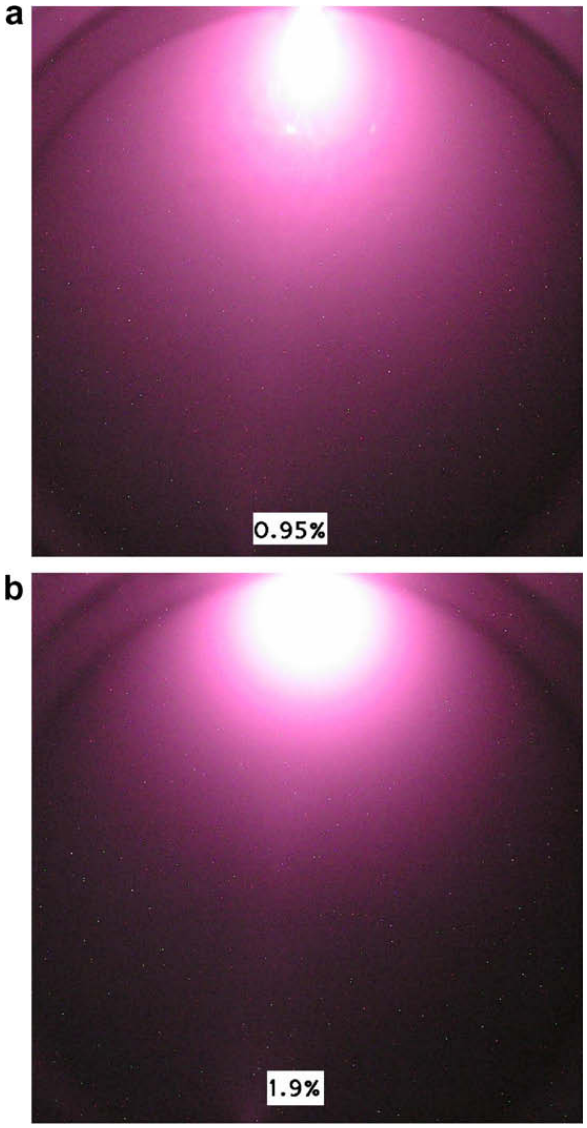

Fig. 11. Photographs of NIR photon density wave for homogenous microsphere phantoms with (a) 0.95% v.d., and (b) 1.9% v.d.

4.3. Numerical image reconstruction

In numerical image reconstruction using acquired intensity data, a homogeneous-background phantom was meshed with 240 elements and 257 nodes, and homogeneous optical-properties were set as an initial guess. For each acceptable reconstructed image, thirty iterations were used, where 2 min per iteration were taken under a host PC with 3.6 GHz Intel Pentium 4 CPU and 3.25 GB RAM. Meanwhile, the relative mean square errors (MSEs) of $(\Delta\Phi)_n$ to $(\Delta\Phi)_0$ reduce to as small as 10^{-2}. Reconstructed tomographic images were obtained by using the developed scheme as described in Section 2. Intensity signals as input of the image-reconstructed scheme were measured surrounding the boundary surface of the heterogeneous Intralipid phantom with one inclusion. To achieve image reconstruction, sixteen streams of data in total were acquired with sixty out-emitted intensities detected surrounding circumference for each incident NIR light. It is worth mentioning that prior to the computation of image reconstruction, system-based offsets resulting from measured data need to be removed. The approach to calibrating these offsets adopts the measured intensity of the heterogeneous phantom associated with the ratio between the computed and measured homogeneous phantom for each observed location, as described below,

$$\Phi_{\text{hetero}}^{\text{computed}} = \frac{\Phi_{\text{homo}}^{\text{computed}}}{\Phi_{\text{homo}}^{\text{measured}}} \times \Phi_{\text{hetero}}^{\text{measured}}. \tag{7}$$

Fig. 14 shows image reconstruction result, where Fig. 14(a) depicts the schematic geometry of the tested phantom with 1-D profiles (c1 and c2) and Fig. 14(b) demonstrates the absorption-coefficient images at the different phases of successive iterations. Fig. 14(c1) 1-D horizontal and Fig. 14(c2) 1-D vertical profiles characterize the computed absorption coefficients by transecting through the original and the final reconstructed images. In 1-D profiles, dot and solid lines indicate the designated and the reconstructed, respectively. Most notably, it is well known that the spatial

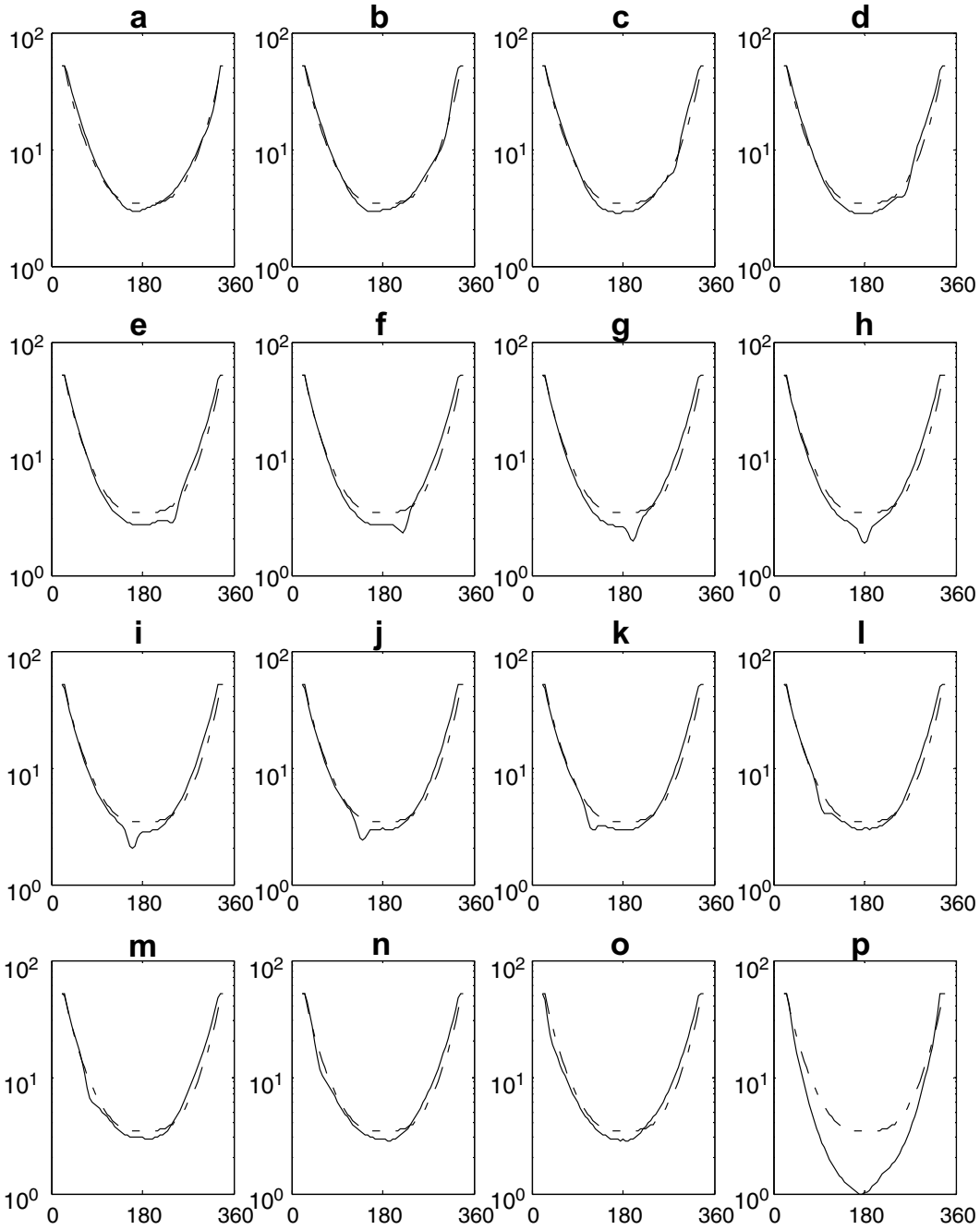

Fig. 12. Demonstration of 1-D measured intensities from the circular Intralipid phantom with one inclusion where intensity vertical axis is in arbitrary unit and angle is horizontal axis from source to detector; for the following, the angle between source and inclusion is (a) 337.5°, (b) 315°, (c) 292.5°, (d) 270°, (e) 247.5°, (f) 225°, (g) 202.5°, (h) 180°, (i) 157.5°, (j) 135°, (k) 112.5°, (l) 90°, (m) 67.5°, (n) 45°, (o) 22.5°, and (p) 0°, respectively.

resolution of NIR tomographic images is limited and also spatially dependent [23,24]. The major consequence of having modest spatial resolution is that finely detailed objects appeared blurred. For example, the circular test heterogeneity with sharply defined edges (top-hat profile) that was used here appears as a circular heterogeneity with a blurred Gaussian-shaped profile. This change in shape will ultimately limit the accuracy of the reconstruction because there is an inherent bias in the image due to the loss of resolution.

In the case, the reconstructed absorption image appears a more accurate representation of the position and shape of the inclusion relative to the reconstructed diffusion image. Compared with the reconstructed absorption image, the reconstructed diffusion image is not evident on the inclusion location due to the ignorance on the effect of the phase function and g factor in the reconstruction algorithm at the current phase, which will be improved by using an imaging system built in the frequency domain in the future.

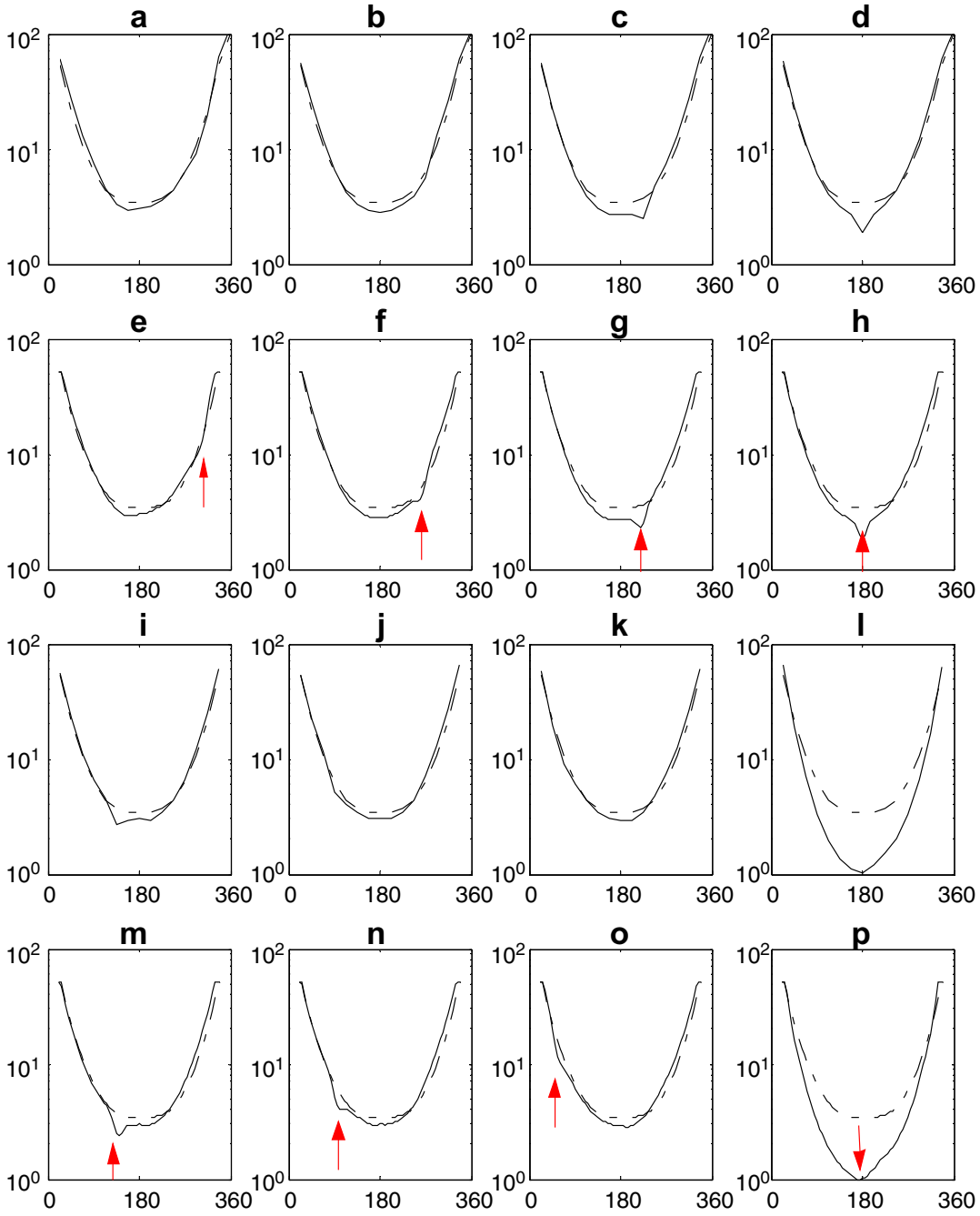

Fig. 13. Comparison of the measuring systems with the fixed 16-source/16-detector pairs (1st and 3rd rows) and the single rotating source and detector (2nd and 4th rows). 1-D measured intensities from the circular Intralipid phantom with one inclusion; the angle between source and inclusion is (a and e) 315°, (b and f) 270°, (c and g) 225°, (d and h) 180°, (i and m) 135°, (j and n) 90°, (k and o) 45°, and (l and p) 0°, respectively.

5. Conclusion

The purpose of this paper is not to perform an exhaustive examination of DOT, but rather to offer an initial assessment of the potential for the DOT imaging system based on a highly angular resolution mechanism. As described in previous sections, it is feasible to build a reliable and economical NIR tomographic imaging system for the clinic use by adopting a single rotating source-and-detector device which is beneficial to the angular resolution of circumferential measurements rather than the system using fixed number of source-and-detector pairs. The experimental measurement of known objects can characterize and justify the performance of the developed system. A numerical method for solving image reconstruction applied to the heterogeneous Intralipid phantom has been demonstrated. Promising results have been obtained, especially for absorption images. Due to the success on both of the instrumentation and inverse computation, the former exhibits a high scanning resolution for likely tiny tumor, and the corresponding necessary resolution can be improved with finer meshes and more nodes used in

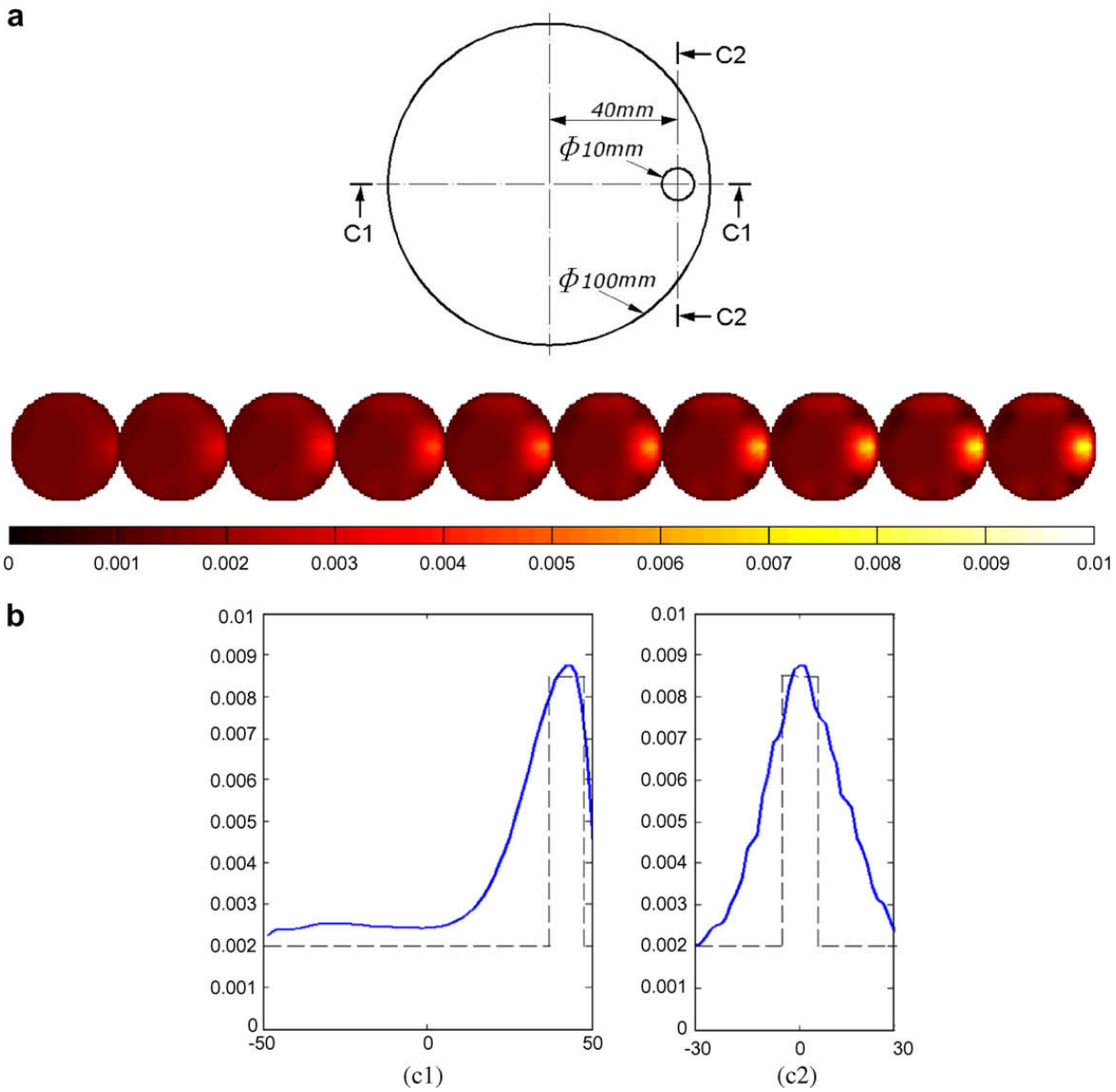

Fig. 14. Demonstration of absorption image reconstruction using experimental data (unit: mm^{-1}). (a) Geometric sketch of the heterogeneous Intralipid phantom tested in the experiment; (b) a series of reconstructed absorption images at the 3rd, 6th, 9th, 12th, 15th, 18th, 21st, 24th, 27th, and 30th iteration, respectively; last one, the 30th iteration, is the final result obtained; (c1 and c2) 1-D horizontal and vertical profiles transecting through the center of the inclusion, where dash line and solid line indicate the target (designated) and the final reconstructed, respectively.

the FEM modeling. It implies that the ability of the developed NIR imaging system is applicable to real medical cases. Furthermore, the optimal resolution for design criteria can be determined and will be investigated in the near future.

Beyond the current study, it is anticipated that an appropriate initial guess closer to the real configuration and the quantitative analysis of the reconstructed optical-property phantom remain to be further investigated. Additionally, the high spatial-frequency information of reconstructed images can be improved with incorporating image super-resolution or the correlation between measured intensities. Also, frequency domain technique will be constructed and performed to precisely determine scattering images in the near future.

Acknowledgements

Authors acknowledge the funding support from the grant by the Veteran General Hospital/University System of Taiwan Joint Research Program (VGHUST95-P4-13, VGHUST96-P4-17), as well as the grants (Project Nos. NSC 93-2218-E-008-007 and NSC 95-2221-E-236-002) from the National Science Council in Taiwan, ROC.

References

[1] B.W. Pogue, H. Jiang, K.D. Paulsen, U.L. Osterberg, Frequency-domain diffuse optical tomography of breast tissue detector size and imaging geometry, in: Proceedings of 19th International Conference on IEEE/EMBS 1997, pp. 2745–2749.

[2] A.H. Hielschera, A.Y. Bluestonea, G.S. Abdoulaeva, A.D. Klosea, J. Laskera, M. Stewart, U. Netzc, J. Beuthanc, Near-infrared diffuse optical tomography, Disease Markers 18 (2002) 313–337.
[3] J.C. Hebden, K.S. Wong, Time-resolved optical tomography, Applied Optics 32 (4) (1993) 372–380.
[4] J.C. Hebden, D.T. Deply, Enhanced time-resolved imaging with a diffusion model of photon transport, Optics Letter 19 (5) (1994) 311–313.
[5] S.R. Arridge, M. Schweiger, Image reconstruction in optical tomography, Philosophical transactions of the royal society a-mathematical physical and engineering sciences 352 (1997) 717–726.
[6] E.M.C. Hillman, Experimental and theoretical investigations of near infrared tomographic imaging methods and clinical applications, Ph.D. thesis of U.C.L., 2002.
[7] E.M.C. Hillman, J.C. Hebden, M. Schweiger, H. Dehghani, F.E.W. Schmidt, D.T. Deply, S.R. Arridge, Time resolved optical tomography of the human forearm, Physics in Medicine and Biology 46 (2001) 1117–1130.
[8] J.C. Hebden, H. Veenstra, H. Dehghani, E.M.C. Hillman, M. Schweiger, S.R. Arridge, D.T. Deply, Three dimensional time-resolved optical tomography of a conical breast phantom, Applied Optics 40 (19) (2001) 3278–3287.
[9] M. Schweiger, S.R. Arridge, Optical tomographic reconstruction in a complex head model using *a-priori* region boundary information, Physics in Medicine and Biology 44 (1999) 2703–2721.
[10] M. Cheng Pan, C.H. Chen, W.H. Huang, M. Chun Pan, C.S. Tseng, NIR image reconstruction using a single-rotating-source/detector scanning device, in: Proceedings of SPIE on Biomedical Optics Conference, vol. 5859, 2005, pp. 99–107.
[11] M. Cheng Pan, W.H. Huang, C.H. Chen, M. Chun Pan, NIR electro-optical measurement for pseudo-models of biological tissues, in: Proceedings of SPIE on Biomedical Optics Conference, vol. 6139, 2006, pp. 171–180.
[12] M.-Chun. Pan, W.H. Huang, Y.L. Shih, M. Cheng Pan, Pseudo-model technique of biological tissues for the development of NIR diffuse optical tomography, Journal of Chinese Institute of Engineers 30 (2) (2007) 189–201.
[13] C.H. Schmitz, M. Locker, J.M. Lasker, A.H. Hielscher, R.L. Barbour, Instrumentation for fast functional optical tomography, Review of Scientific Instruments 73 (2) (2002) 429–439.
[14] C.H. Schmitz, H.L. Graber, H. Luo, I. Arif, J. Hira, Y. Pei, A. Bluestone, S. Zhong, R. Andronica, I. Soller, N. Ramirez, S.S. Barbour, R.L. Barbour, Instrumentation and calibration protocol for imaging dynamic features in dense-scattering media by optical tomography, Applied Optics 39 (34) (2000) 6466–6486.
[15] K.D. Paulsen, H. Jiang, Spatially varying optical property reconstruction using a finite element diffusion equation approximation, Medical Physics 22 (1995) 691–701.
[16] R. Choe, Diffuse optical tomography and spectroscopy of breast cancer and fetal brain, Ph.D. thesis, University of Pennsylvania, 2005.
[17] T.M. McBride, B.W. Pogue, E.D. Gerety, S.T. Poplack, U.L. Österberg, K.D. Paulsen, Spectroscopic diffuse optical tomography for the quantitative assessment of hemoglobin concentration and oxygen saturation in breast tissue, Applied Optics 38 (25) (1999) 5480–5490.
[18] H. Jiang, K.D. Paulsen, U.L. Österberg, B.W. Pogue, M.S. Patterson, Optical image reconstruction using frequency-domain data: simulations and experiments, Journal of the Optical Society of America A – Optics Image Science and Vision 13 (1996) 253–266.
[19] F.E.W. Schmidt, Development of a time-resolved optical tomography system for neonatal brain Imaging, Ph.D. thesis of U.C.L., 1999.
[20] M. Chun Pan, W.H. Huang, C.H. Chen, M. Cheng Pan, Development and system characteristics of diffuse optical tomography using single rotating-source/detector mechanism, in: Proceedings of SPIE on Biomedical Optics Conference, 2006, pp. 60800D-1–60800D-8.
[21] D. Mangiardi, A. Plesco, L. Romito, D. Thakker, Reduction of hemoglobin. Available from: http://www.seas.upenn.edu/courses/belab/LabProjects/1998/BE309F98M2R01.htm.
[22] H.J. Van Staveren, C.J.M. Mose, J. Van Marie, S.A. Prahl, M.J.C. Van Gemert, "Light scattering in intralipid-10% in the wavelength range of 400–1100 nm, Applied Optics 30 (31) (1991) 4507–4514.
[23] B.W. Pogue, T.O. McBride, J. Prewitt, U.L. Osterberg, K.D. Paulsen, Spatially variant regularization improves diffuse optical tomography, Applied Optics 38 (13) (1999) 2950–2961.
[24] S.C. Davis, H. Dehghani, P.K. Yalavarthy, B.W. Pogue, K.D. Paulsen, Comparing two regularization techniques for diffuse optical tomography, in: Book of Optical Tomography and Spectroscopy of Tissue VII (Britton Chance et al.), in: Proceedings of SPIE 6434, 64340X, 2007.